Geophys. J. Int. (2009) **177,** 878–890 doi: 10.1111/j.1365-246X.2009.04129.x

Inversion of torsional oscillations for the structure and dynamics of Earth's core

Bruce A. Buffett,[1] Jon Mound[2] and Andrew Jackson[3]

[1] *Department of Earth & Planetary Science, University of California, Berkeley, CA* 94720*, USA. E-mail: buffett@geosci.uchicago.edu*
[2] *School of Earth & Environment, University of Leeds, Leeds, UK*
[3] *Institut für Geophysik, ETH Zürich,* CH-8093 *Zürich, Switzerland*

Accepted 2009 January 23. Received 2009 January 23; in original form 2008 October 3

SUMMARY

Oscillations in Earth's liquid core with periods of several decades are inferred from variations in the magnetic field. The observed periods are consistent with a type of hydromagnetic wave known as torsional oscillations. These oscillations represent a set of very-low-frequency normal modes in which the internal magnetic field provides the primary restoring force. By adapting the methods of normal-mode seismology, we construct estimates for the internal structure of the magnetic field and several other key parameters, including the viscosity of the inner core. The structure of the recovered field provides useful insights into the nature of convection. We find evidence of columnar convection in the core, and estimate the strength of the field generated by these flows ($\approx$0.3 mT). We also use the normal modes to recover the excitation source for the oscillations. Much of the excitation appears to originate near the surface of a cylinder that is tangent to the equator of the inner core. Distinct events rise above a background level of excitation, and may be related to instabilities in the geodynamo.

Key words: Inverse theory; Geomagnetic induction; Theoretical seismology.

1 INTRODUCTION

Seismic observations are routinely used to make inferences about the internal structure of Earth. 3-D estimates of elastic properties and attenuation can be recovered from measurements of body waves, surface waves and elastic-gravitational free oscillations (Romanowicz 2003). Information about the source mechanisms can also be obtained (Gilbert & Dziewonski 1975). Seismic methods have also been applied to measurements of acoustic waves in the Sun (Gough *et al.* 1996), where the excitation is thought to be a result of turbulent convection (Goldreich & Keeley 1977). Successful application of inverse methods in both seismology and helioseismology motivate the search for other applications using different types of waves. In this study, we focus on long-period waves in Earth's core, where a combination of gravity, rotation and magnetic forces provide the necessary restoring forces (Acheson & Hide 1973).

Wave motion at the top of the core can be detected through variations in Earth's magnetic field. Horizontal motion near the boundary disturbs the radial component of the main field, which diffuses through the mantle to the Earth's surface on timescales of a few years or less (Backus 1983; Courtillot *et al.* 1984). When the period of the wave motion is longer than the diffusion time we anticipate a contribution to the observed variation in the magnetic field. By combining observations of field variations with a physical description of the waves in the core, we attempt to recover physical properties that govern the propagation and excitation of these waves.

Variations in the magnetic field are correlated with changes in the length of day on timescales of several decades (Vestine & Kahle 1968; Braginsky 1984; Roberts *et al.* 2007). Torsional oscillations are expected to have the period and spatial structure needed to explain both the magnetic field and length-of-day variations (Braginsky 1970). The spatial form of the waves is controlled by the influence of rotation, which causes fluid motion to be nearly geostrophic. The spherical geometry of the core constrains the geostrophic flow to follow lines of latitude with no spatial variations in the direction of the rotation axis. Conservation of mass imposes an additional constraint by prohibiting spatial variations in the direction of flow. Consequently, a geostrophic flow can be described by the motion of nested cylinders that align with the rotation axis (see Fig. 1). Each cylinder is labelled by its distance s from the rotation axis, and the motion of adjacent cylinders is coupled by the s-component of magnetic field, which threads across the surface of these cylinders. Differential motion between cylinders shears the magnetic field, creating a restoring force for the waves. Coupling between the fluid and the surrounding mantle and inner core can also affect the period and damping of the waves.

The geostrophic structure of the waves also means that torsional oscillations carry angular momentum. Each cylinder moves with a velocity that is specified by the zonal part of the flow at the core surface. When the flow in the interior is geostrophic, the velocity at the core surface suffices to determine the velocity over the entire cylinder. Jault *et al.* (1988) and Jackson *et al.* (1993) use this approximation to calculate the axial angular momentum of the core

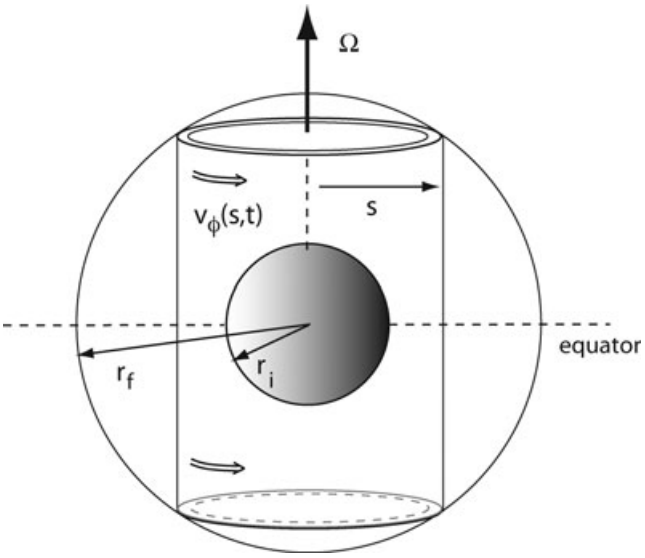

Figure 1. Schematic illustration of geostrophic flow in Earth's fluid core. The zonal flow v_ϕ is constant on the surfaces of cylinders that align with the rotation axis Ω. Each cylinder is identified by the distance s from the rotation axis. The radii of the core–mantle and inner-core boundaries are denoted by r_f and r_i, respectively.

from time-dependent estimates of zonal flow at the core surface. Temporal changes in the core angular momentum require commensurate changes in the rotation of the mantle to conserve total angular momentum. The changes in mantle rotation can be detected in observations of the length of day (Stephenson & Morrison 1995; Gross 2001). Good agreement between the predictions and the observations supports the use of the geostrophic approximation, and suggests that the motion of cylinders can be reliably determined from the zonal flow at the core surface.

More recent studies have sought to make quantitative inferences from the spatial and temporal patterns of fluid flow at the core surface. Several authors (Jault *et al.* 1996; Hide *et al.* 2000; Pais & Hulot 2000) have reported evidence for wave-like motion in the core, which they attribute to torsional oscillations. Other studies have shown that torsional oscillations can contribute to short-period variations in the magnetic field, including the phenomena of geomagnetic jerks (Bloxham *et al.* 2002; Wardinski *et al.* 2008). These short-period field variations appear to be correlated with changes in length of day (Holme & de Viron 2005), consistent with expectations for torsional oscillations. All of these studies support the existence of torsional oscillations in the core (Braginsky 1984) and provide important details about the form of the waves.

A more direct connection to torsional oscillations was made in the studies of Zatman & Bloxham (1997, 1999). These authors represented the time-dependent core flow using two waves with specified period and damping. Both the period and spatial structure of these waves were used to invert for the s-component of the internal magnetic field and a friction coefficient at the core–mantle boundary (CMB). (The friction term served as both a sink and a source for the waves, depending on the sign of the friction coefficient.) This work established a new direction for research and highlighted a number of important questions. For example, the period and spatial form of the waves could reasonably be interpreted as free oscillations (e.g. the normal modes of the system). All of these waves should reflect a common set of physical parameters that govern the wave motion. However, there is no guarantee that the procedure of fitting waves to the observed core flow respects this dependence on a single set of parameters. Discrepancies in the basic parameters that determine the waves can be accommodated by allowing for different sources of excitation. In fact, the study of Zatman & Bloxham (1999) recovered very different friction coefficients for the two waves. Different choices for the structure, period or even the number of the waves would likely yield very different friction coefficients for each wave (e.g. different excitations). A key challenge in both the previous and this work lies in separating the structure of the waves from the source of excitation.

Another challenge arises from the limited spatial resolution of the observations (Hulot *et al.* 1992). Uncertainties in the crustal field limit the resolution of magnetic field models at the CMB. When flows are determined from temporal changes in the field models, the limited resolution is propagated into the velocity field. The issue of spatial resolution is important because the actual structure of a wave may be different from the structure inferred from magnetic observations, even for waves with the longest period. A direct comparison between the core flow and the predicted waves can yield spurious results because the structure of the waves is not adequately resolved by the observations. Filtering the model predictions to the same resolution as the core flow before making comparisons makes a substantial difference in the inversion results.

In this study, we use a Green's function to predict the wave motion excited by an impulsive source in the core or mantle (Buffett & Mound 2005). The response to a distributed source (in both space and time) is obtained by convolving the Green's function with an appropriate source function. This representation demonstrates a fundamental non-uniqueness between the physical properties that determine the Green's function and the source function that excites the waves. One strategy for separating these effects relies on a subdivision of the input core flow into shorter time intervals. Incremental changes in the flow over several decades can be approximated using the free motion of the core, as described by a linear combination of normal modes. This approximation is valid when the excitation over the interval of interest is small. By iteratively adjusting the parameters that define the normal modes (and hence the Green's function) we can successively improve the fit to the observations. This fitting procedure yields one set of parameter estimates for the Green's function. Repeating the fitting procedure over each subdivision of the flow model gives redundant estimates, which can be compared to assess the consistency of the procedure. A consistent set of parameters is used to construct the Green's function. The entire record of core flow is then used to recover the source function with a known Green's function.

In Section 2, we begin in with a brief discussion of the flow at the surface of the core. Models of flow from Jackson (1997) are used as the primary input in the inversion (effectively the 'observations'). The uncertainty in the flow model is most naturally expressed in terms of a spherical harmonic decomposition, so we transform the predicted wave motion into a set of time-dependent spherical harmonic coefficients. This procedure provides a natural way to filter the predicted wave motion to the same spatial resolution as the core flow. In Section 3 we briefly introduce the Green's function, and identify the parameters that are included in the inversion. A two-stage inversion strategy is developed in Section 4. We initially recover the parameters that define the Green's function. In the second stage, we retrieve the source function in both space and time. Information recovered from this inversion has a number of consequences, which are explored in Section 5. Conclusions are drawn in Section 6.

2 FLOW AT THE SURFACE OF THE CORE

Estimates of fluid motion at the top of the core are based on time variations in the magnetic field. Under the frozen flux hypothesis (Roberts & Scott 1965), the induction equation for the radial magnetic field B_r reduces to

$$\frac{\partial B_r}{\partial t} = -\nabla_h \cdot (v B_r), \tag{1}$$

where v is the fluid velocity and ∇_h is the horizontal gradient operator. Both B_r and $\partial B_r/\partial t$ are estimated at the CMB by downward continuing the potential field at the Earth's surface. Flows that satisfy (1) are not unique and must be constrained by other conditions to reduce the ambiguity (Bloxham & Jackson 1991; Voorhies 1995). A commonly used constraint is based on the assumption of tangential geostrophy (Hills 1979; LeMouël 1984), which requires a leading-order balance between the horizontal components of the Coriolis force and the pressure gradient. Such a balance is valid when the horizontal components of the Lorentz force, viscous force and inertia (in the rotating frame) are all small near the CMB. The resulting condition on the velocity requires

$$\nabla_h \cdot (v \cos\theta) = 0, \tag{2}$$

where θ is the colatitude (see LeMouël 1984). The flows obtained by Jackson (1997) are fit to the secular variation in (1), subject to the condition in (2). Values for B_r and $\partial B_r/\partial t$ are taken from model ufm1 of Bloxham & Jackson (1992). A regularization is also imposed in the inversion to penalize high-frequency spatial and temporal variations in the flow. Different levels of regularization were used to determine three flow models (denoted by uvm-r, uvm-i, uvm-s). The heaviest smoothing is imposed in model uvm-s, whereas the roughest model is uvm-r. We adopt the smoothest model over the entire interval of the record (e.g. 1840–1990). We have also experimented with the roughest model over the interval 1950–1990, but the results for the Green's function are not substantially altered.

All of the flow models are represented by

$$\mathbf{v} = \nabla \times (\mathcal{T}\mathbf{r}) + \nabla_h(r\mathcal{P}), \tag{3}$$

where $\mathcal{T}$ and $\mathcal{P}$ are the usual toroidal and poloidal scalars. Both $\mathcal{T}$ and $\mathcal{P}$ are expressed in spherical coordinates (r, θ, ϕ) and expanded in Schmidt quasi-normalized spherical harmonics, $Y_l^m(\theta, \phi)$, in the form

$$\mathcal{T} = \sum_{l,m} t_{lm}(t) Y_l^m(\theta, \phi) \tag{4}$$

$$\mathcal{P} = \sum_{l,m} p_{lm}(t) Y_l^m(\theta, \phi), \tag{5}$$

where $\{t_{lm}, p_{lm}\}$ are the time-dependent coefficients that define the flow. Flows associated with torsional oscillations involve only a subset of these coefficients. Such flows have only an azimuthal component, $v_\phi \equiv v \cdot \hat{\phi}$ with no dependence on longitude ϕ. In this case the toroidal–poloidal decomposition reduces to

$$v_\phi(\theta, t) = -\frac{\partial \mathcal{T}}{\partial \theta} = -\sum_l t_{l0}(t) \frac{\partial Y_l^0}{\partial \theta}, \tag{6}$$

where the summation over l is restricted to odd values because of the symmetry of the velocity about the equator. Fig. 2 shows $v_\phi(\theta, t)$ as a function of $\sin\theta$ for the period 1840–1990. This flow is specified at 5-yr intervals and the spatial resolution is limited by the truncation imposed on the series in (6). The flow model of Jackson (1997) is truncated at $l = 14$. We remove the time average from $v_\phi(\theta, t)$ prior to fitting the Green's function.

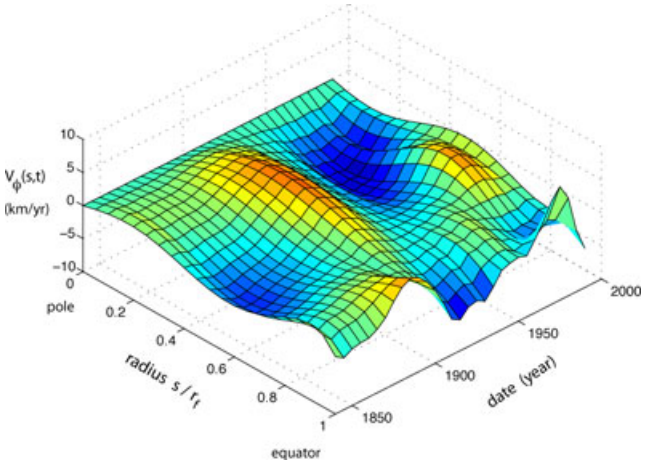

Figure 2. Linear velocity of fluid cylinders $v_\phi(s, t)$ as a function of radius s and time t from model uvm-s (Jackson 1997). We use the variations about the time average $\bar{v}_\phi(s)$ as the input flow model for determining the Green's function and excitation source.

Error estimates for the coefficients t_l^0 are obtained from the covariance matrix that results from the linear inverse problem for determining the flow. Errors on the input secular variation, as well as the damping, affect these *a posteriori* errors. We take the square root of the variances (from the diagonal elements of the covariance matrix) and ignore the covariances. The standard deviations (or formal errors) for t_l^0 in 1980 are shown in Fig. 3. A general decrease in the formal error with increasing l is due primarily to the regularization. Small-scale flow is suppressed by the regularization, so the recovery of flow at large l is required to fit the observed secular variation. However, the need for flow at large l depends on both the accuracy and spatial resolution of the magnetic secular variation. Changes in the resolution of the secular variation are suggested by changes in the behaviour of coefficients t_{l0} over time (see Fig. 4). Coefficients t_{10}, t_{30} and t_{50} exhibit large oscillations over most of the record, whereas t_{70} and t_{90} are relatively small at early times. This

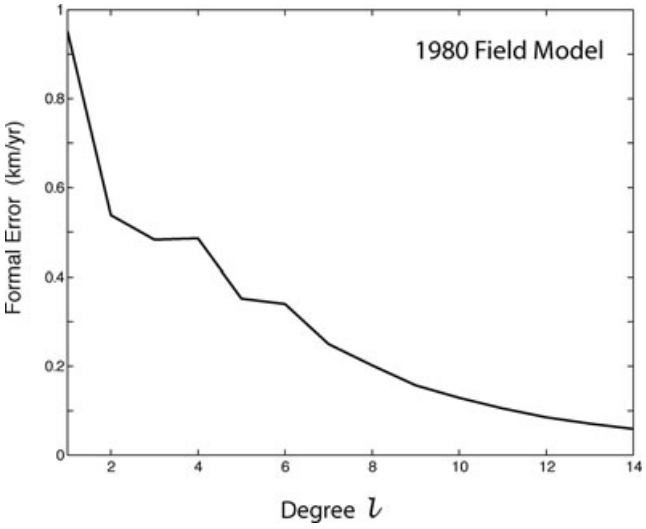

Figure 3. Formal error on the zonal coefficients t_l^0 for the flow model in 1980. The decrease in formal error with increasing l is due to the regularization used in the inversion of field variations for the surface core flow.

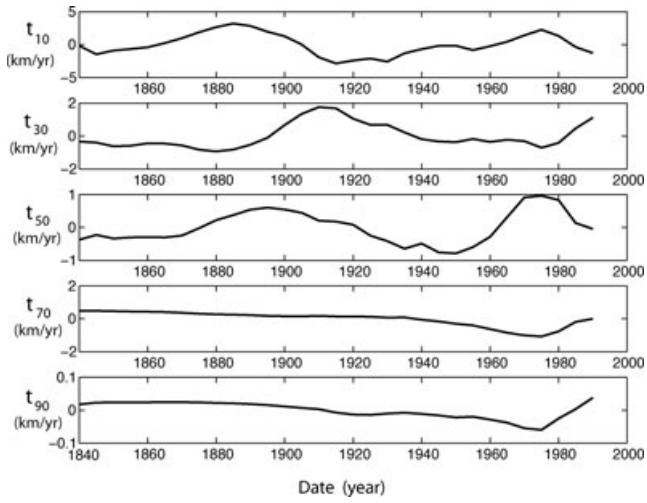

Figure 4. Temporal variations in the zonal coefficients t_l^0 for odd $l = 1$ to 9. Oscillations are not evident in coefficients t_7^0 and t_9^0 prior to 1940.

result suggests that the measurements do not require components of flow with $l = 7$ and 9, at least at early times. Larger variations in t_{70} are evident in the last 40 yr of the flow models, where the spatial resolution of the magnetic field model is probably the best. Changes in the resolution of the input flow model can adversely affect our inversion if these uncertainties are not accurately represented. We avoid the question of time-dependent uncertainties by confining our attention to the first three spherical harmonic components of the flow, where wave-like motion is observed over the entire record.

Redundant estimates of the Green's function are obtained by subdividing the flow model into three 60-yr intervals. We exclude the first 10 yr, and subdivide the remainder into intervals 1850–1910, 1890–1950 and 1930–1990. A modest overlap permits slightly longer intervals, which is useful for estimating the Green's function. Because there is little evidence of torsional oscillations in t_{70} prior to 1930, we restrict the input flows to components t_{10}, t_{30} and t_{50} for all three time intervals. The Green's function is filtered to the same resolution as the flow model, prior to calculating a misfit between the prediction and the flow model. The parameters of the Green's function (see Section 3) are iteratively adjusted to improve the fit over each segment of the record.

Practical considerations guide the choice of weights used to fit the input flow models. The formal errors on the input flow suggest that the highest weight is given to coefficients with the largest value of l. This means that most weight in our calculation is given to t_{50}, whereas least weight is given to t_{10}. On the other hand, we do not use t_{70} to estimate the Green's function, even though it has a relatively small formal error. Consequently, the formal errors are not treated consistently for all parts of the flow. We deal with the question of errors (or weights) by comparing the results of several strategies. In one case, we adopt weights based on the formal errors for coefficients t_{10}, t_{30} and t_{50}. In the other case, we assign equal weight to each spherical harmonic component. To avoid any unintended contribution from the normalization of Y_l^m, we transform the representation in (6) to fully normalized spherical harmonics when equal weights are given to the coefficients. Comparison of results obtained with these two weighting schemes show that the differences are relatively small. Larger differences are found when estimates from the three subsets of the input flow are compared. Consequently, we report the parameter values obtained using the formal errors with Schmidt quasi-normalized harmonics.

3 GREEN'S FUNCTION FOR TORSIONAL OSCILLATIONS

A mathematical description of the waves is needed to relate the flow at the core surface to physical properties in the interior of the core. We use a Green's function to describe the response of the fluid core, inner core and mantle to an impulsive excitation (Buffett & Mound 2005). Time-dependent motions of the inner core and mantle are described by angular velocities $u_i(t)$ and $u_m(t)$, respectively, whereas $u_{\rm f}(s,t)$ represents the angular velocity of fluid cylinders as a function distance s from the rotation axis. The linear velocity at the core surface is defined by $v_\phi = s u_{\rm f}(s,t)$, where $s = r_{\rm f}\sin\theta$ and $r_{\rm f}$ is the radius of the core surface. When an impulsive source is applied at $s = s'$ and $t = t'$, the motion at time $t > t'$ can be expressed as a linear combination of normal modes

$$u_{\rm f}(s,s',t-t') = \sum_{k=1}^{\infty} c_k(s')\tilde{u}_{\rm f}^k(s)\mathrm{e}^{-\mathrm{i}\omega_k(t-t')} \tag{7}$$

$$u_m(s',t-t') = \sum_{k=1}^{\infty} c_k(s')\tilde{u}_m^k\mathrm{e}^{-\mathrm{i}\omega_k(t-t')} \tag{8}$$

$$u_i(s',t-t') = \sum_{k=1}^{\infty} c_k(s')\tilde{u}_i^k\mathrm{e}^{-\mathrm{i}\omega_k(t-t')}, \tag{9}$$

where $\tilde{u}^k \equiv [\tilde{u}_{\rm f}^k(s), \tilde{u}_m^k, \tilde{u}_i^k]$ is the eigenfunction of the kth normal mode, ω_k is the complex frequency for this mode and the constant c_k depends on the location of the source. A source in the fluid core at $s = s'$ yields

$$c_k = -\omega_k\tilde{u}_{\rm f}^k(s') \tag{10}$$

whereas a source in either the mantle or inner core gives

$$c_k = -\omega_k\tilde{u}_m^k \quad \text{or} \quad -\omega_k\tilde{u}_i^k. \tag{11}$$

The expressions for c_k in (10) and (11) correct a sign error in Buffett & Mound (2005).

Physical properties of the core enter the problem through the structure and frequency of the normal modes. One of the primary restoring forces for the waves is due to magnetic tension between the fluid cylinders. This property depends on the mean-square value of the B_s field over the surface of the cylinders. We denote this mean-square field by $\{B_s^2\}$, and represent the s-dependence of the rms field $\{B_s^2\}^{1/2}$ using an expansion in (fully normalized) Legendre polynomials $\bar{P}_n$

$$\{B_s^2\}^{1/2} = \sum_{n=0}^{N} b_n\bar{P}_n(x), \tag{12}$$

where b_n are the constant coefficients and $x = 2(s/r_{\rm f}) - 1$ varies from -1 to 1 on the interval $s = 0$ to $r_{\rm f}$. We truncate the expansion for $\{B_s^2\}^{1/2}$ at $N = 4$, which restricts the inversion to the first five coefficients. An equivalent expansion for $\{B_s^2\}$ would require $N = 8$. In either case the truncation limits the spatial complexity of $\{B_s^2\}$.

Another restoring force is due to gravitational coupling between the inner core and the mantle. The gravitational torque on the inner core can be described by (Buffett 1996)

$$\Gamma_i = \gamma(\omega)(\varphi_m - \varphi_i), \tag{13}$$

where φ_m and φ_i are angular deviations of the inner core and mantle from their position of static equilibrium and $\gamma(\omega)$ is a frequency-dependent amplitude. The angular velocities of the mantle and inner

core are defined by $u_m(i) = \mathrm{d}\varphi_m/\mathrm{d}t$ and $u_i(t) = \mathrm{d}\varphi_i/\mathrm{d}t$. The frequency dependence of $\gamma(\omega)$ arises when the shape of the inner core is allowed to adjust by viscous flow over the period of an oscillation. When the adjustment occurs over a characteristic time τ, the frequency-dependent amplitude is given by (Buffett 1998)

$$\gamma(\omega) = \gamma(\infty)\left[1 + \frac{i}{\omega\tau}\right]^{-1}, \tag{14}$$

where the unrelaxed amplitude $\gamma(\infty)$ depends on the distribution of mass in the mantle and the shape of the inner core. For computational reasons (see Appendix A) it is convenient to expand (14) as a power series in $\omega\tau$. Rearranging (14) in the form

$$\gamma(\omega) = \frac{-\mathrm{i}\gamma(\infty)\omega\tau}{(1 - \mathrm{i}\omega\tau)} \tag{15}$$

we approximate $\gamma(\omega)$ as

$$\gamma(\omega) = -\mathrm{i}\omega\tau\gamma(\infty) + \omega^2\tau^2\gamma(\infty) \tag{16}$$

which is valid when $\omega\tau \ll 1$. The influences of $\gamma(\infty)$ and τ on the motion are difficult to separate at typical frequencies for torsional oscillations because the quadratic term $(\omega\ \tau)^2$ in (16) is usually quite small. This means that the inversion recovers the product $\tau\gamma(\infty)$ more easily than the individual components τ and $\gamma(\infty)$. A independent estimate of $\gamma(\infty)$ and τ was given by Mound & Buffett (2006), who attributed a 6-yr oscillation in the length of day to a gravitational oscillation between the core and the mantle. Fitting the period and damping of the oscillation to a simple model yields $\gamma(\infty) = 3 \times 10^{20}$ N m and $\tau > 5$ yr. Given the limitations noted above we set $\gamma(\infty) = 3 \times 10^{20}$ and treat τ as a parameter in the inversion.

Coupling at the fluid–solid boundaries also affects to the normal modes. Separate contributions at the surfaces of the mantle and inner core can be view as a friction of the form

$$f_m(s) = \mathcal{F}_m(s)[u_\mathrm{f}(s) - u_m] \tag{17}$$

$$f_i(s) = \mathcal{F}_i(s)[u_\mathrm{f}(s) - u_i], \tag{18}$$

where the amplitudes $\mathcal{F}_m$ and $\mathcal{F}_i$ depend on the coupling mechanism. Magnetic coupling is important at the inner-core boundary due to the high electrical conductivity on either side of the boundary. Even a modest radial field of 0.5 mT is sufficient to bind the fluid cylinders to the inner core over periods typical of torsional oscillations. Any cylinder in contact with the inner core tends to rotate as a quasi-rigid body at the angular velocity of the inner core. As a consequence, the normal modes have little sensitivity to magnetic tension (and hence $\{B_s^2\}$) for values of s inside the tangent cylinder (i.e. the cylinder that is tangent to the equator of the inner core). We return to this point when interpreting the estimate for $\{B_s^2\}$.

We also include magnetic coupling at the CMB. This coupling depends on both the conductance of the mantle and the strength of the radial magnetic field [denoted $B_\mathrm{r}(s)$]. We adopt a constant mantle conductance of $C = 5 \times 10^7$ S and recover the amplitude of $B_\mathrm{r}(s)$ as a parameter in the inversion. The amplitude of $B_\mathrm{r}(s)$ is represented by a single parameter because the spatial structure (e.g. the s-dependence) is prescribed. We consider separately the cases of a dipole field, $B_\mathrm{r}(s) = B_\mathrm{r}\sqrt{1 - s^2}$, and a spatially uniform field, $B_\mathrm{r}(s) = B_\mathrm{r}$. The latter is intended to represent a radial field that is dominated by small-scale components. In either case the value recovered for B_r depends on the choice of C because the strength of magnetic coupling at the CMB is proportional to the product CB_r^2.

Magnetic coupling at the CMB also affects the boundary conditions for the normal modes. At $s = r_\mathrm{f}$ we require (Buffett & Mound 2005)

$$\frac{\partial\tilde{u}_\mathrm{f}^k}{\partial s} = \mathrm{i}\omega_k(\tilde{u}_\mathrm{f}^k - \tilde{u}_m^k)\mu_0 C B_\mathrm{r}^2/\{B_s^2\}, \tag{19}$$

where μ_0 is the permeability of free space. Adopting a dipole field for B_r requires $\partial\tilde{u}_\mathrm{f}^k/\partial s = 0$ at the equator, whereas a constant radial field means that $\partial\tilde{u}_\mathrm{f}^k/\partial s \neq 0$ when C is not zero. A discrete approximation to (19) is imposed in all calculations by requiring $\tau(s)$ to vanish at $s = r_\mathrm{f}$ in a finite volume representation of the governing equations. Independent estimates for B_r^2 and $\{B_s^2\}$ are recovered by fitting the input flow. Thus we allow the inversion to determine the appropriate boundary conditions. However, we can always enforce the equality of B_r^2 and $\{B_s^2\}$ at the equator by adjusting the value assumed for C. Identical boundary conditions and normal modes are obtained using different values for B_r^2 and C as long as the product CB_r^2 is unchanged.

Table 1. Parameters of earth model.

Parameter	Value
Density of core ρ_f	10^4 kg m^{-3}
Electrical conductivity σ_f	5×10^5 S m^{-1}
Radius of fluid core r_f	3480 km
Radius of inner core r_i	1221 km
Moment of mantle C_m	7.12×10^{37} kg m^2
Moment of inner core C_i	5.87×10^{34} kg m^2

A number of other parameters also contribute to the frequency and spatial structure of the normal models. The list includes the density and electrical conductivity of the fluid core, the moments of the inner core and mantle, and the radii of the inner-core boundary and CMB. All of these parameters are relatively well known and can be treated as constants (see Table 1). More poorly known parameters include $\{B_s^2\}$, $\gamma(\infty)$, τ and B_r at the CMB. Another poorly known parameter is the value of B_r at the inner-core boundary. However, forward modeling shows that the normal modes are relatively insensitive to B_r at the inner-core boundary once this field exceeds 0.5 mT. Since the field at the inner-core boundary likely exceeds 0.5 mT, we exclude this parameter from the fitting procedure. Consequently, the parameter estimation is restricted to $\{B_s^2\}$, τ and B_r, recalling that we cannot easily separate the contributions of τ and $\gamma(\infty)$. When five coefficients b_n are used to represent $\{B_s^2\}^{1/2}$ in (12), we have a total of seven parameters. We seek to determine these seven parameters for each 60-yr interval of core flow. The flow in each interval (from model uvm-s) is represented by coefficients t_{10}, t_{30} and t_{50} at 13 epochs, corresponding to a total of 39 'observations'.

4 INVERSION METHOD

A two-step procedure is used to recover the Green's function and the excitation source from the input flow models. A Green's function is determined in the first step by fitting a linear combination of normal modes to the input core flow over three 60-yr intervals. The resulting Green's function is used in the second step to estimate the source function $S(s', t')$ as a function of space s' and time t' over the entire time interval of the input flow.

4.1 Estimating the Green's function

The Green's function in (7)–(9) describes the response of the Earth to an impulsive excitation at $s = s'$ and $t = t'$. The subsequent motion for $t > t'$ is represented by a linear combination of normal

models, where the coefficients c_k are specified by the location of the excitation. The definitions in (10) and (11) are based on the assumption that the system is initially at rest. This representation needs to be generalized to the case of a non-stationary initial condition. In general, it is always possible to represent the motion using a linear combination of modes, although the amplitude and phase of the coefficients c_k may change when an excitation occurs. Over a short interval where the accumulated excitation is small, we might treat coefficients c_k as constants. This approximation would be appropriate for a low level of excitation that produces small relative changes in c_k over the interval in question. On the other hand, a large impulsive event can produce substantially changes in c_k, requiring distinct coefficients before and after the event. Unfortunately, we do not know in advance when (or if) these events occur. The wave-like structure of the flow model suggests that the excitation over one period is not too large, so we proceed with the assumption that the input flow model over a 60-yr interval can be fit by a set of normal modes with constant coefficients c_k. Once the coefficients are determined by least squares we can assess the misfit between the predicted flow and the input flow model for each 60-yr interval. A poor misfit is taken to mean that the parameters used to compute the modes require improvement. Iterative adjustments to the model parameters are made to minimize the misfit using a downhill simplex method (e.g. Press *et al.* 2007). Once the Green's function is determined from each of the three 60-yr intervals, we can look for evidence of a large excitation by examining the consistency of the recovered parameters. A large event might be expressed by an anomalous estimate for some of the recovered parameters. Parameters from this interval could be excluded in constructing a time-averaged Green's function. Ultimately, we can use the recovered source function $S(s, t)$ to assess the consistency of our interpretation.

Several measures of misfit are possible. For example, we could compute the rms discrepancy between the predicted and 'observed' fluid velocity $v_\phi(s, t) = s\, u_{\rm f}(s, t)$ on a grid in both s and t. Alternatively, we could convert the predicted values of $v_\phi(s, t)$ into a set of spherical harmonic coefficients $t_{l0}(t)$ using the orthogonality of spherical harmonics. In this case the misfit is given by the rms discrepancy between the predicted and 'observed' coefficients $t_{l0}(t)$. The latter approach has the advantage of effectively filtering the prediction to the same spatial resolution as the input core flow. In addition, the weights used to fit the linear combination of modes to the input core flow are most naturally expressed in terms of $t_{l0}(t)$ rather than $v_\phi(s, t)$. We proceed by converting the predicted angular velocity $u^k_{\rm f}(s, t)$ of each normal mode into a linear velocity v^k_ϕ. Next, we compute the spherical harmonic coefficients $t^k_{l0}(t)$ for each mode using

$$t^k_{l0}(t) = -\frac{(2l+1)}{2(l+1)l}\int_0^\pi v^k_\phi P_{l1}(\cos\theta)\sin\theta\,{\rm d}\theta, \qquad (20)$$

where $\theta = \sin^{-1}(s/r_{\rm f})$ and $\partial Y^0_l/\partial\theta$ is rewritten in terms of associated Legendre functions $P_{l1}(\cos\theta)$. Finally, we express the 'observed' harmonic coefficients as a linear combination of the modal coefficients t^k_{l0},

$$t_{l0}(t_i) = \sum_{k=1}^{n} c_k t^k_{l0}(t_i)\,, \qquad (21)$$

for each epoch t_i in the time interval and each l in the input flow model. The (complex) constants c_k are obtained by least squares, and the predicted motion is reconstructed using (7)–(9). An illustrative comparison of the observed and predicted motion is shown in Fig. 5 for the time interval 1850–1910 using three normal modes in (21). For this particular example the parameter values for $\{B_s^2\}^{1/2}$, τ and $B_{\rm r}$ have been iteratively adjusted to minimize the misfit (see Table 2). The definition of the misfit used in the inversion is simply the weighted sum of square errors in the coefficients $t_{l0}(t)$. The weights for each t_{l0} are the inverse of the variances for model uvm-s. A comparison of the observed and predicted coefficients t^0_l is shown in Fig. 6 for each subdivision of the input flow model.

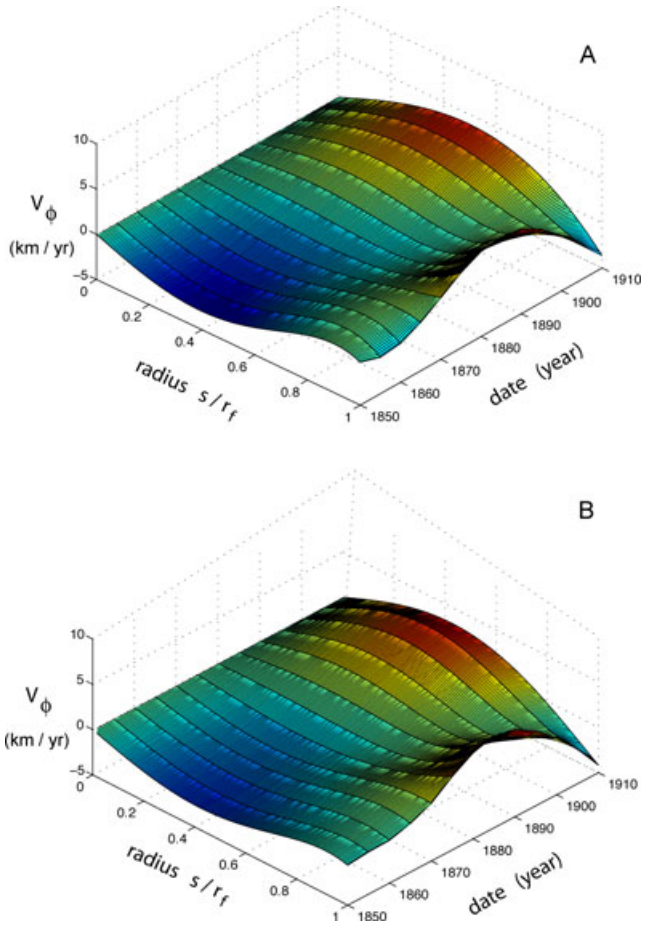

Figure 5. Comparison of input (a) and predicted (b) fluid motion for the interval 1850–1910. The parameters of the Green's function have been iteratively adjust to minimize the misfit.

Table 2. Parameter estimates for Green's function.

Parameter	Units	1850–1910	1890–1950	1930–1990
b_0	mT	0.393	0.323	0.248
b_1	mT	−0.157	−0.282	−0.046
b_2	mT	−0.016	0.287	0.127
b_3	mT	−0.079	−0.237	−0.132
b_4	mT	0.168	0.177	0.092
$B_{\rm r}^{\rm dip}$	mT	0.25	0.29	0.21
$B_{\rm r}^{\rm con}$	mT	0.15	0.18	0.20
τ	yr	5.9	1.7	0.7

Redundant estimates of the parameter values are recovered from each 60-yr interval. Fig. 7 shows the estimates for $\{B_s^2\}^{1/2}$. For each time interval we constrain $\{B_s^2\}^{1/2}$ at $s = r_{\rm f}$ to equal the (observed) rms value of $B_{\rm r}(s)$ at $s = r_{\rm f}$. The latter is computed numerically by integrating $B_{\rm r}^2$ from the gufm1 model (Jackson *et al.* 2000) over a band of latitudes centred at the equator. As the band of latitudes narrows around the equator, the rms radial field in 1980 approaches

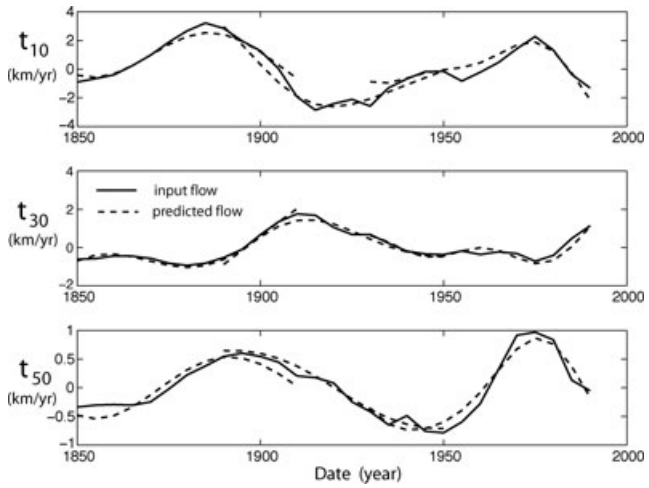

Figure 6. Comparison of predicted and input flow coefficients $t_l^0(t)$ for three subdivisions of the flow model (in units of km yr^{-1}). Weights for the fitting the input flow model are based on the formal errors for uvm-s.

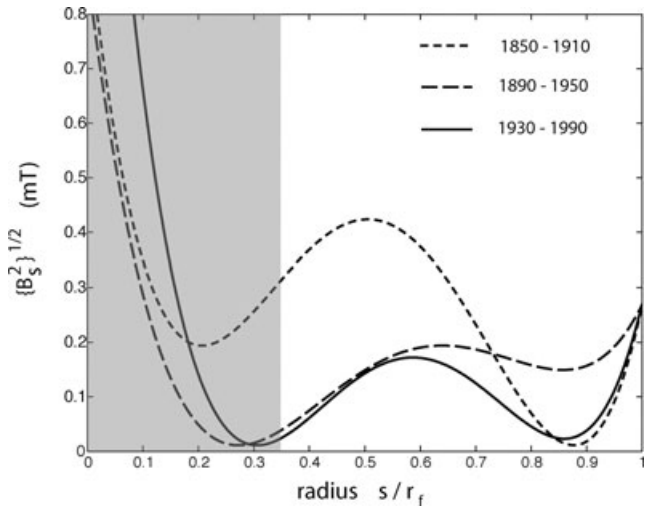

Figure 7. Estimates of $\{B_s^2\}^{1/2}$ recovered from three subdivisions of the input flow model. The shaded region denotes the interior of the tangent cylinder where fluid cylinders terminate on the surface of the inner core. Little significance is attached to the estimates of $\{B_s^2\}^{1/2}$ inside $s/r_\mathrm{f} = 0.35$ because the fluid is strongly coupled to the inner core by magnetic stresses. Outside the tangent cylinder we find two local maxima in each estimate of $\{B_s^2\}^{1/2}$. One maximum occurs at $s/r_\mathrm{f} = 1$ and the other occurs in the interval $s/r_\mathrm{f} = 0.5$–0.6.

a constant value of $B_\mathrm{r}^\mathrm{rms} = 0.268$ mT. Values at other times can vary by as much as 15 per cent, although we do not attempt to adjust the constraint over time in the inversion. The rms value of B_r at the equator is geometrically equivalent to $\{B_s^2\}^{1/2}$ at $s = r_\mathrm{f}$. Imposing this condition on $\{B_s^2\}^{1/2}$ (at the value in 1980) improves the stability of the inversion and yields much less variability when the number of modes is increased. (We typically use 3 modes for reasons described below.) In addition, we find better agreement between the estimates of $\{B_s^2\}^{1/2}$ for each time intervals. A caveat is that the value of $B_\mathrm{r}^\mathrm{rms}$ inferred from surface observations may underestimate the true field because short-wavelength components are not detected at the surface. Allowing for short-wavelength field could potentially increase $\{B_s^2\}^{1/2}$ at $s = r_\mathrm{f}$ relative to that shown in Fig. 7.

Individual estimates of $\{B_s^2\}^{1/2}$ from each of the three subsets of input flow have common features, although they differ somewhat in amplitude. For example, all three estimates decrease into the core from the fixed value at $s/r_\mathrm{f} = 1$, creating a local minimum within a narrow range of radius ($s/r_\mathrm{f} \approx 0.85$–$0.88$). A second local minimum is found in all three estimates just inside the tangent cylinder (e.g. the shaded region inside $s/r_\mathrm{f} = 0.35$), where the fluid cylinders terminate on the surface of the inner core. The estimates of $\{B_s^2\}^{1/2}$ also have a local maximum, roughly in the range $s/r_\mathrm{f} \approx 0.5$–$0.6$, although the maximum value differs in the three cases. We attach little significance to the estimates inside the tangent cylinder where the modes have little sensitivity to $\{B_s^2\}^{1/2}$. The fluid tends to corotate with the solid inner core due to strong magnetic coupling at the inner-core boundary, which limits the role of $\{B_s^2\}^{1/2}$ as a restoring force for the motion. Outside the tangent cylinder the average magnitude of $\{B_s^2\}^{1/2}$ is surprisingly weak, typically less than the observed value at $s/r_\mathrm{f} = 1$.

In assessing the differences between the three estimates of $\{B_s^2\}^{1/2}$, we see no evidence for an anomalous interval. Estimates from intervals 1850 to 1910 and 1930 to 1990 are quite similar near $s/r_\mathrm{f} \approx 1$, whereas the estimates from 1890 to 1950 and 1930 to 1990 are similar just outside the tangent cylinder. We consider two approaches for combining these individual estimates into a single Green's function. In one case, we simply average the parameter estimates from each interval. This approach defines an average Green's function. We also recover a single set of parameters by fitting the entire record of input flow with a linear combination of modes (e.g. no subdivision of the input flow model). We subsequently refer to this Green's function as the single estimate. Both the average and single estimate for $\{B_s^2\}^{1/2}$ are shown in Fig. 8. We also show the estimate from the study of Zatman & Bloxham (1997) and a prediction from the geodynamo model of Matsui & Okuda (2004). The average and single estimate for $\{B_s^2\}^{1/2}$ are surprisingly similar to each other, suggesting that constant modal coefficients (and hence weak

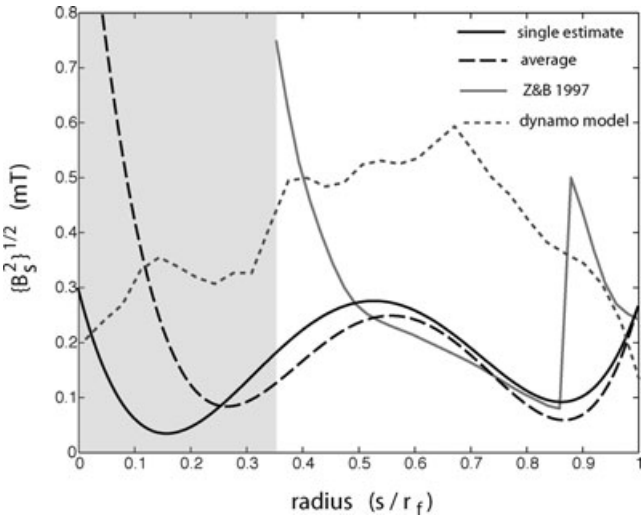

Figure 8. A composite estimate of $\{B_s^2\}^{1/2}$ obtained by fitting the entire input flow model to a single estimate of the Green's function or by averaging individual estimates from the subdivision of the input flow model. Both approaches yield similar results. We also show the estimate of Zatman & Bloxham (1997), which was restricted to the region outside the tangent cylinder and a prediction from the geodynamo model of Matsui & Okuda (2004).

excitation) is a reasonable approximation. We return to the estimate from the geodynamo model in Section 5.

The estimate of Zatman & Bloxham (1997) differs most from our result in the region near the tangent cylinder and again near $s/r_{\rm f} = 0.9$. Our estimate of the field is somewhat lower on average (nominally 0.2 mT versus 0.3 mT for Zatman & Bloxham 1997), although there is surprising agreement in the region between $s/r_{\rm f} = 0.5$ and 0.85. However, the structure of $\{B_s^2\}^{1/2}$ is quite different. When we use the estimate of $\{B_s^2\}^{1/2}$ from Zatman & Bloxham (1997) to calculate normal modes, we find that the waves bear little resemblance to the input flow model. Steep gradients in the estimate of $\{B_s^2\}^{1/2}$ (particularly near $s/r_{\rm f} \approx 0.9$) cause large spatial variations in the amplitude of the waves, which are not evident in the input flow. In those regions the friction coefficient (and hence the source term) must modify the motion in order to fit the input flow. It follows that the source term plays an important role in the dynamics. We have argued in favour of a small source on the basis of the good agreement between average and single estimate of $\{B_s^2\}^{1/2}$. Thus it is possible that the differences between the estimates of $\{B_s^2\}^{1/2}$ in this study and that of Zatman & Bloxham (1997) are due to the handling of the source term.

Values for the field coefficients b_n and model parameters $B_{\rm r}$ and τ are listed in Table 2. Estimates for $B_{\rm r}$ are given for two different structures of radial field at the CMB (i.e. a dipole and a constant field). Differences in the structure of the CMB field have little affect on the values of $\{B_s^2\}^{1/2}$ and τ. However, the amplitude of the radial field is altered by the spatial structure; a smaller radial field is preferred when a constant field is adopted. The amplitude of $B_{\rm r}$ in either case is lower than the value that would be inferred from recent IGRF models (Maus *et al.* 2005), where the rms radial field at the CMB in spherical harmonic degrees $l \leq 13$ is 0.31 mT. Recall that magnetic coupling depends on both $B_{\rm r}^2$ and the conductance C of the lower mantle, so better agreement with the observed field seems to require a reduced mantle conductance. Our estimates for τ are somewhat lower than the bound inferred by Mound & Buffett (2005), particularly for the interval 1930–1990. On the other hand, the three estimates for τ exhibit large variability, which we take to represent the uncertainty.

Another useful measure of uncertainty is given by the sensitivity of the predicted flow to the model parameters. We assess the sensitivity by computing the change in the misfit to the input flow as the model parameters are altered from their optimal values. As an example, we consider the increase in misfit for the first interval 1850–1910 (see Fig. 9). The changes in $\{B_s^2\}^{1/2}$, $B_{\rm r}^{\rm dip}$ and τ are reported as a fractional change (in percent). In assessing the sensitivity to $\{B_s^2\}^{1/2}$ we simply scale the amplitude of the field without altering the s-dependence. A large change in the misfit for a particular choice of parameter indicates a large sensitivity. It is clear from Fig. 9 that the normal modes are most sensitive to $\{B_s^2\}^{1/2}$ and much less sensitive to τ and $B_{\rm r}^{\rm dip}$. Less sensitivity permits larger changes in the parameter values without substantially altering the misfit. Thus it is possible to find acceptable fits with larger or smaller values for $B_{\rm r}$ and τ. Recently, Dumberry & Mound (2008) have shown that the radial field and conductance proposed to explain observations of the Earth's nutations (Buffett *et al.* 2002) cause damping times for the torsional oscillations to be shorter than the predicted period. Such overdamped waves are not found in this study (see Table 3), which suggests that the radial field and conductance inferred from nutations are too high to be compatible with the interpretation of the core flow in terms of free torsional oscillations.

We conclude this section by presenting the spatial form of the normal modes for the single-estimate parameter values (specifically

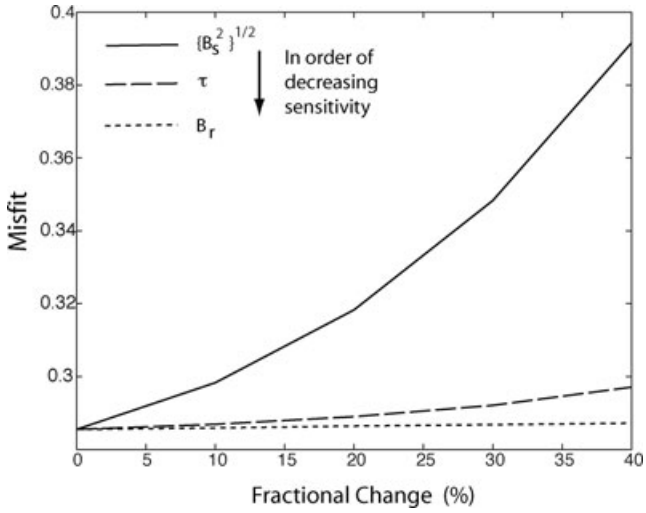

Figure 9. Changes in the misfit between the observed and predicted flow as the model parameters are varied from the optimal values. The misfit is most sensitive to $\{B_s^2\}^{1/2}$ and least sensitive to $B_{\rm r}$ in the vicinity of the optimal estimates for the Green's function parameters.

Table 3. Period P_i and damping time D_i of the first four normal modes using the single estimate and average Green's functions.

Time (yr)	Single	Average
P_1	86.3	109.6
P_2	42.9	49.2
P_3	30.6	34.4
P_4	23.6	26.8
D_1	505	1128
D_2	441	809
D_3	362	523
D_4	314	415

using a dipole field at the CMB). In Fig. 10, we show the linear velocity $v_\phi(s)$ and a filtered version of the flow that includes only coefficients t_1^0, t_3^0 and t_5^0 in the spherical harmonic expansion, consistent with the resolution of the input flow model. Much of the short-wavelength structure of the modes is lost when the flow is filtered. Higher order modes begin to look like lower order modes, so the system of equations for fitting the modes to the input flow becomes ill-conditioned if too many modes are included. Using three modes to fit the input flow gives a good compromise between accuracy and instability. Adding a fourth mode makes very little difference for the recovered parameters, while a fifth mode often makes the linear system of equations ill-conditioned. We have restricted our calculations to three modes to reduce instabilities in the inversion for the source function.

4.2 Source function

Several sources of dissipation are included in the description of the normal modes. Magnetic coupling at both the CMB and inner-core boundary acts like a friction, which damps the modes. Dissipation also results from viscous adjustment of the inner core. Each source of dissipation contributes to the imaginary part of the eigenfrequency ω_k, thereby causing a gradual decay in the free motion with time. Some form of excitation is required to sustain the waves. The goal of this section is to recover the source function from the

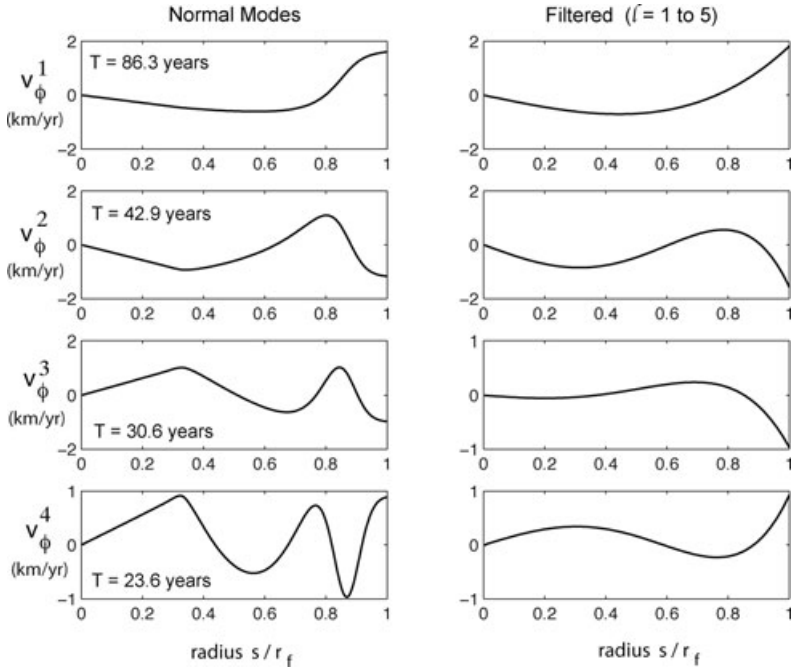

Figure 10. Spatial structure of the first four normal models calculated using the single estimate of the Green's function. The left panel shows the linear velocity $v_\phi^k(s)$, whereas the right panel shows the structure of the same modes filtered to the resolution of the input flow model. We give the predicted period T for all four modes, although we include only the first three when inverting for the Green's function.

input flow model using the Green's functions from the previous section.

A general solution for the flow due to torsional oscillations is obtained by convolving the Green's function with a suitable source function. In principle, the source can reside anywhere in the core or mantle. Different possibilities yield different expressions for the change in the constants c_k (see eqs 10 and 11). We express the solution for flow in the outer core as

$$u_{\rm f}(s,t) = u_{\rm f}^0(s,t) + \int_{t_0}^{t}\int_0^{r_{\rm f}} u_{\rm f}(s,s',t-t')S(s',t')\,{\rm d}s'{\rm d}t', \qquad (22)$$

where $u_{\rm f}(s, s', t - t')$ is the Green's function for the fluid part of the response and $S(s', t')$ is the source function. The function $u_{\rm f}^0(s, t)$ represents the initial set of waves that would be present if $S(s', t')$ vanished in (22). Analogous expressions for the response of the mantle and inner core are based on $u_m(s', t - t')$ and $u_i(s', t - t')$ in (8) and (9).

The source function $S(s', t')$ in (22) can be recovered from the input flow model $u_{\rm f}(s, t)$ when the Green's function is prescribed. It is clear from (22) that a different Green's function would yield a different source function. This is the motivation for a two-step inversion. The initial state in (22) is obtained by fitting the normal modes to the input flow model at t_0 (specifically 1850). The fitting procedure determines a set of coefficient for the normal modes. (Three modes are used to fit the input flow, consistent with the number of modes used to represent the Green's function.) Once the coefficients are determined the unforced motion $u_{\rm f}^0(s, t)$ can be predicted at later times. The input flow model $u_{\rm f}(s, t)$ gradually evolves away from $u_{\rm f}^0(s, t)$, and the difference can be used to estimate $S(s', t')$. We discretize the source function using a series of delta functions in time

$$S(s',t') = S_1(s')\delta(t'-t_1) + S_2(s')\delta(t'-t_2) + ..., \qquad (23)$$

where t_p (for $p = 1$ to N) are chosen to coincide with the times of the input flow model and $S_p(s')$ is the amplitude of the excitation at t_p. Each amplitude $S_p(s')$ describes the spatial distribution of the excitation at that particular time. We seek to determine the set of functions $S_p(s')$ that reproduce the input flow model $u_{\rm f}(s, t)$ using a prescribed Green's function $u_{\rm f}(s, s', t - t')$.

To illustrate we consider the calculation of S_1 at $t = t_1$. On substituting (23) in (22), the solution for $u_{\rm f}(s, t)$ at t_1 can be written as

$$u_{\rm f}(s,t_1^+) = u_{\rm f}^0(s,t_1) + \int_0^{r_{\rm f}} u_{\rm f}(s,s',0)S_1(s')\,{\rm d}s', \qquad (24)$$

where t_1^+ denotes the time immediately after the excitation. (We drop the superscript + below for the sake of simplicity.) A discrete approximation of the integral in (24) is given by

$$\int_0^{r_{\rm f}} u_{\rm f}(s,s',0)S_1(s')\,{\rm d}s' \approx \sum_{j=1}^{n} u_{\rm f}(s_i,s'_j,0)S_1(s'_j)\Delta s'_j, \qquad (25)$$

where $s_j (j = 1, n)$ define the gridpoints. We subsequently use $S_1^j \equiv S_1(s'_j)\ \Delta s_j$ to denote the torque on the jth cylinder at time t_1. Consequently, the solution at $t = t_1$ can be approximated by

$$u_{\rm f}(s_i,t_1) = u_{\rm f}^0(s_i,t_1) + \sum_{j=1}^{n} u_{\rm f}(s_i,s'_j,0)S_1^j. \qquad (26)$$

When the excitation resides in the fluid outer core the discrete form of the Green's function is a $n \times n$ matrix, where each element (i, j) is given by

$$u_{\rm f}(s_i,s'_j,0) = \sum_{k=1}^{m} \omega_k \tilde{u}_{\rm f}^k(s_i)\tilde{u}_{\rm f}^k(s'_j). \qquad (27)$$

This expression is simply a discrete representation of (7) using the coefficients defined in (10). Linear superposition of the forced and free motion defines the total flow in (26). In general, the solutions for $u_{\rm f}(s_i, t_1)$ and $u^0_{\rm f}(s_i, t_1)$ can be represented at $t = t_1$ using a linear combination of normal modes. We restrict this representation to the first m modes

$$u_{\rm f}(s_i, t_1) = \sum_{k=1}^{m} c^1_k \tilde{u}^k_{\rm f}(s_i) {\rm e}^{-{\rm i}\omega_k(t_1 - t_0)} \tag{28}$$

$$u^0_{\rm f}(s_i, t_1) = \sum_{k=1}^{m} c^0_k \tilde{u}^k_{\rm f}(s_i) {\rm e}^{-{\rm i}\omega_k(t_1 - t_0)} \tag{29}$$

and note that the coefficients c^1_k and c^0_k may be different. Substituting (27)–(29) into (26) yields a single algebraic condition for each mode by virtue of the orthogonality of the normal modes. We obtained for the kth mode

$$c^1_k - c^0_k = \sum_{j=1}^{n} \omega_k \tilde{u}^k_{\rm f}(s'_j) S^j_1 {\rm e}^{{\rm i}\omega_k(t_1 - t_0)} \tag{30}$$

with similar conditions for all m modes in the Green's function. When this set of conditions is written in matrix form, we obtain the linear system

$$\Delta c = M S_1, \tag{31}$$

where M is an $m \times n$ matrix and S_1 is an $n \times 1$ source vector at $t = t_1$. Each row of M corresponds to an eigenfunction of a normal mode [e.g. $\tilde{u}^k_{\rm f}(s'_j)$] multiplied by a complex constant $\omega_k {\rm e}^{{\rm i}\omega_k(t_1 - t_0)}$. The elements of the column vector Δc specify the differences in the coefficients c_k for each mode before and after the excitation at $t = t_1$. The coefficients at each time can be obtained by fitting the input flow model to m normal modes. Thus the elements of Δc and M are ultimately set by the definition of the Green's function.

Conservation of angular momentum places another constraint on S_1 because an internal source cannot exert a net torque on the Earth as a whole. When the source is confined to the fluid outer core, we require

$$\sum_{j=1}^{n} S^j_1 = 0 \tag{32}$$

which can be appended as an extra linear condition in (31). In effect, the $(m + 1)$th row of an expanded M matrix has elements equal to ζ, and the $(m + 1)$th element of the augmented Δc vector is set to zero. We use $\zeta = 10^6$ to ensure that (32) is fit almost exactly. We solve this augmented system of equations for S_1 by minimizing the misfit $\epsilon_1 = MS_1 - \Delta c$, subject to a regularization condition on the amplitude of S_1. Specifically, we minimize

$$\Phi = (MS_1 - \Delta c)^T (MS_1 - \Delta c) + \lambda S^T_1 S_1, \tag{33}$$

where λ is a scalar constant that can be adjusted to obtain a suite of solutions with different penalties on the amplitude of S_1. The value of λ is chosen to be large enough to stabilize the inversion, but small enough that the solution is relatively insensitive to changes in λ. In practice, we increase the value of λ until a consistent spatial pattern emerges for S_1. The solution for S_1 is given by

$$S_1 = (M^T M + \lambda I)^{-1} M^T \Delta c. \tag{34}$$

Source functions S_p at other times $t = t_p$ are inferred from $\Delta c = c^p_k - c^{p-1}_k$ using the same value for λ.

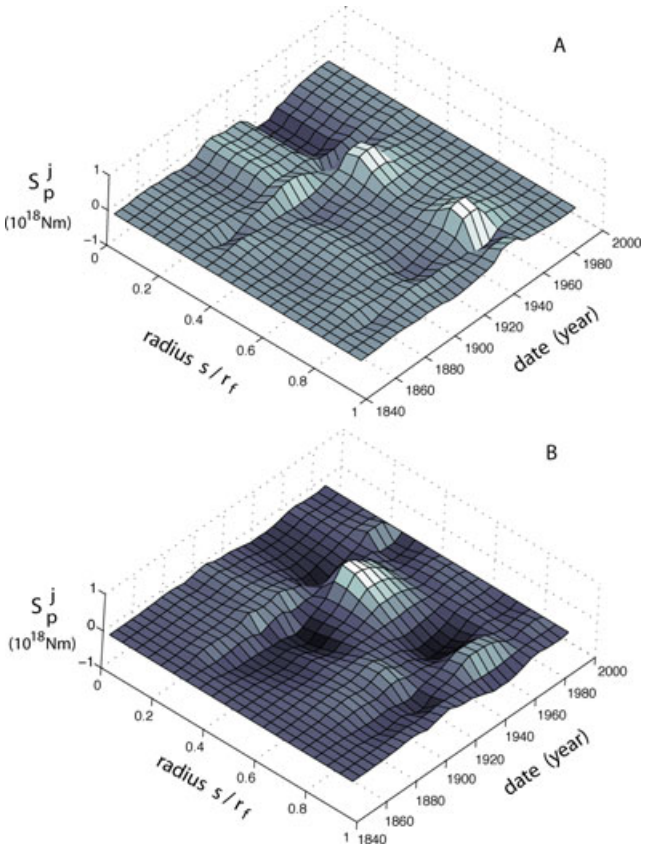

Figure 11. Estimates of the source function $S^j_p = S(s'_j, t'_p)\Delta s_j$ obtained using the (a) average and (b) single estimate of the Green's function. The amplitude of the source is expressed in units of 10^{18} N m.

Tests on synthetic data motivate our procedure for recovering the source function from (34). First, we determine the modal coefficients c^p_k at each epoch t_p by fitting the normal modes to an interval of time around the point of interest. We typically use 30 yr of flow to recover a reliable estimate for c^p_k. The point of interest, t_p, coincides with the centre of the 30-yr interval, except when the intervals occur near the ends of the data record. Second, we reduce the resolution of the source function by interpolating the eigenfunctions $\tilde{u}^k_{\rm f}(s_j)$ onto a coarser grid. We use a grid with $n = 150$ to calculate the normal modes, but interpolate these functions onto a coarser grid prior to constructing the matrix M. A coarse grid with $n = 20$ is sufficient to resolve the features of the first three modes.

Fig. 11 shows the discrete source function $S^j_p \equiv S(s'_j, t'_p)\Delta s_j$ obtained using the average and the single estimate of the Green's function. Differences in the two Green's functions cause distinct features in the recovered source function, but the general structure is broadly similar. A large excitation event in both estimates occurs in 1940–1945. A peak in the excitation occurs just outside the tangent cylinder and a second peak with variable amplitude occurs near the equator. The time dependence of the excitation inside the tangent cylinder is similar in the two estimates, and there is also general agreement on the low level of excitation prior to 1900. The amplitude of the excitation is also consistent, although this is largely a function of the regularization imposed in the inversion.

It is important to emphasize that the source function depends on the choice of Green's function. We cannot rule out the possibility that part or all of the excitation in Fig. 11 is a consequence of errors in either the Green's function or the input flow model. Errors in the

Green's function are expected to cause wave-like sources, which would compensate for errors in the eigenfrequencies or eigenfunctions of the modes. We find some evidence for periodic variations in the source inside the tangent cylinder, which would be compatible with errors in the Green's function. However, we also find relatively abrupt excitations outside the tangent cylinder, particularly in Fig. 11(a), where there is little evidence for periodic variations before and after the event. This behaviour argues against an error in the Green's function. A similar claim is less compelling for the large excitation in Fig. 11(b), although there is no comparable amplitude in the excitation outside the tangent cylinder at earlier or later times, as expected if the source was due primarily to errors in the Green's function. Random errors in the input flow model are an alternative explanation for the recovered source function. Such errors might cause erratic excitations in both space and time. Instead, we find relatively little excitation during the early part of the record. Thus if random errors in the flow model cause the excitations shown in Fig. 11, it is somewhat surprising that these errors are conspicuously absent prior to 1900.

5 DISCUSSION

Estimates for the Green's function and excitation source provide unique insights into the structure and dynamics of the core. The most sensitive parameter in the Green's function is $\{B_s^2\}^{1/2}$. Possible mechanisms for generating $\{B_s^2\}^{1/2}$ are interpreted using the results of a numerical geodynamo model. The peak in $\{B_s^2\}^{1/2}$ from the geodynamo model of Matsui & Okuda (2004) (see Fig. 7) coincides with the location of strong helical flow in columns outside the tangent cylinder. This flow lifts and twists a field oriented in ϕ direction to produce a distorted field with both s and z components. We find a similar peak in the recovered $\{B_s^2\}^{1/2}$ at $s/r_{\rm f} \approx 0.5$, which could be explained by centring columns of helical flow at this distance. Vertical columns at this location would reach the CMB at a latitude of 60°. Convergent flow into convective downwelling is expected to produce local patches of radial flux at the CMB (Christensen *et al.* 1998), which are consistent with high-latitude features observed in the radial field (Bloxham & Gubbins 1987). Thus the location of the high-latitude flux patches is compatible with the position of the helical flow we infer from the structure of $\{B_s^2\}^{1/2}$. There is also evidence for strong patches of radial flux near the equator (Jackson 2003). The intensity of these patches is comparable to the high-latitude patches, although the origin of these features is not well understood. We have used the radial field near $s/r_{\rm f} \approx 1$ to constrain $\{B_s^2\}^{1/2}$ at the equator, so the intensity of the field is no surprise. However, it is surprising that the strength of $\{B_s^2\}^{1/2}$ near the CMB is comparable to the value in the interior. This result contrasts with the predictions of the geodynamo model, where the largest value of $\{B_s^2\}^{1/2}$ occurs near $s/r_{\rm f} \approx 0.7$. Our estimate for $\{B_s^2\}^{1/2}$ suggests that the locus of helical flow in the core is closer to the tangent cylinder than that predicted by the geodynamo model, and that the field induced by this flow is somewhat weaker. It also appears that the mechanism responsible for the equatorial flux patches is not operative in the geodynamo model. In our estimate the rapid decrease in $\{B_s^2\}^{1/2}$ from the equator into the core suggests that the equatorial flux patches do not penetrate deeply into the core.

The source function also provides important insight, although the specific conclusions are less certain. The excitation is probably related to instabilities in the geodynamo, and these effects appear to be localized in time. The largest event in Fig. 11(a) is confined to a 10-yr interval. Given the temporal averaging required to estimate the change in modal coefficients, it is possible that this event is even shorter in duration. Several mechanisms could potentially cause this excitation. Field reconnection across thin shear layers (like the Stewartson layer at the tangent cylinder) might be viable if the Lorentz force can change on timescales to explain the abrupt events. It is also possible that the instabilities are primarily hydrodynamic. Shear or baroclinic instabilities across the tangent cylinder might arise from small differences in flow or density across this surface. There also appears to be an excitation source that operates near the equator. One path forward is to identify specific mechanisms that can produce these excitation events. Numerical dynamo models may offer insights in the mechanisms that produce the excitation events (Dumberry & Bloxham 2003). Physical constraints on the spatial and temporal structure of the excitation could be built into the inversion strategy to reduce the degrees of freedom. In the present study we have imposed no constraints on the spatial structure of the source. We merely reduce the spatial resolution of the source and introduce a regularization condition to penalizes the amplitude. Many other inversion strategies are possible. The relative merits of each is likely to depend on the physical processes responsible for the instability.

The amplitude of the source function recovered in this study is nominally 10^{18} N m. Comparable torques are required to explain long-period fluctuations in length of day, although there is no direct connection between the source and the torque on the mantle. Our inversion assumes that $S(s, t)$ produces no net torque on the core. With no change in the angular momentum of the core there can be no change in the angular momentum of the mantle. Instead, the source function generates waves in the fluid that couple to the motion of the inner core and mantle through a combination of magnetic friction, gravitational torques and possibly other coupling mechanisms. The most important coupling mechanism in our calculations is due to gravitational coupling (also see, Mound & Buffett 2005). Without this mechanism the angular momentum of the core is nearly conserved and the angular velocity of the mantle in all of the normal modes is very small. Thus the mantle torque is an intrinsic part of the normal modes and the Green's function.

A joint inversion of length-of-day observations and core flow models could potentially improve the determination of the Green's function. An alternative strategy would be to invert core flow models that are already constrained to satisfy the observed variations in length of day (Holme 1998). One of the likely consequences of such a procedure is to change the spherical harmonic coefficients of the predicted flow. Much of the expected change would occur in coefficients $t_1^0(t)$ and $t_3^0(t)$, which determine the angular momentum of the core. Jault *et al.* (1988) and Jackson *et al.* (1993) have shown that changes in core angular momentum are sufficient to explain long-period variations in the length of day, particularly in the last few decades. Adding length-of-day observations to the inversion for the Green's function would potentially reduce the misfit to coefficients $t_1^0(t)$ and $t_3^0(t)$ by requiring better agreement with the core angular momentum. By contrast, our use of formal errors for the input flow gives most weight to $t_5^0(t)$ and allows larger misfits to $t_1^0(t)$. Small changes in weighting have only a small effect on the recovery of $\{B_s^2\}^{1/2}$, but other parameters may be more sensitive. For example, the inner-core relaxation time τ is poorly constrained in the inversion even though it contributes to the gravitational torque on the mantle and accounts for most of the angular momentum changes in the core. The average value for τ in Table 2 is lower than the preferred estimates of Mound & Buffett (2006). This result may explain why the predicted variation in length-of-day, based on the Green's function and excitation source from this study, accounts

for only half of the observed fluctuations. By jointly fitting the core flow and length-of-day variations, we can expect to improve the sensitivity to parameters that contribute to core–mantle coupling.

6 CONCLUSIONS

We combine a time-dependent model of flow at the top of the core (Jackson 1997) and a simple theory for torsional oscillations (Buffett & Mound 2005) to estimate the internal structure of the magnetic field and several other relevant parameters, including the viscosity of the inner core. We find a local maximum in the cylindrically averaged root-mean-square B_s field (denoted $\{B_s^2\}^{1/2}$) outside the tangent cylinder. We interpret this feature in terms of helical flow in columns at a distance $s/r_f \approx 0.5$ from the rotation axis. (The tangent cylinder is located at $s/r_f = 0.35$.) Vertical columns at this location reach the CMB at a latitude of 60°, which coincides with the location of high-latitude flux patches (Bloxham & Gubbins 1987). These flux patches are thought to represent the ends of convection columns in the core, so the internal structure of the $\{B_s^2\}^{1/2}$ field appears to be consistent with the morphology of the radial field at the CMB. The average strength of the internal field induced by the columnar convection is about 0.3 mT, assuming that the s-component of this induced field is representative. Local values of B_s^2 could be larger, but the cylindrical average is surprisingly weak.

A second local maximum in $\{B_s^2\}^{1/2}$ is found near the equator at the CMB. This feature coincides with another region of strong flux patches in the radial field (Jackson 2003). Our estimate for $\{B_s^2\}^{1/2}$ decreases sharply away from the CMB, suggesting that the equatorial flux patches do not penetrate deeply into the core. Elsewhere in the core the value of $\{B_s^2\}^{1/2}$ is weak.

Estimates for the viscous relaxation time τ of the inner core exhibit large variability (0.7–5.9 yr), but the average value is lower than the preferred values of Mound & Buffett (2006). The dependence of the waves on τ arises primarily through the gravitational torque, which permits changes in the angular momentum of the input core flow. Coefficients $t_1^0(t)$ and $t_3^0(t)$ in the input flow model determine the angular momentum of the core. Time variations in these coefficients require some mechanism to transfer angular momentum to the inner core and mantle. Gravitational torques are the principal coupling mechanism in our calculations. Normal modes computed without this mechanism yield little time variations in the rotation of the mantle (Mound & Buffett 2005). However a prediction for the length-of-day variation underestimates the observed variation by a factor of two, possibly because of the low value for τ and the reduced gravitational torque. We attribute this shortcoming to the use of formal errors, which give most weight on coefficient t_5^0 and allow larger misfit in t_1^0 and t_3^0. A joint inversion of the core flow and length-of-day variations could potentially improve the predictions for the Green's function.

We also recover estimates for the source function that excites the waves. Specific details depend on the choice of Green's function, but many common features are evident in the two estimates reported in this study. A large excitation event in both estimates occurs in 1940–1945. One of the peaks in the excitation occurs near the tangent cylinder and a second occurs near the equator. We also find general agreement on the low level of excitation prior to 1900 and again after the large excitation in 1940–1945. We speculate that the excitation is a result of instabilities in the geodynamo. A better understanding of viable instability mechanisms would constrain the spatial structure of the source and potentially improve the reliability of the inversion results.

ACKNOWLEDGMENTS

We thank Mathieu Dumberry and an anonymous reviewer for thorough reviews and constructive comments that improved the paper. Hiroaki Matsui kindly computed $\{B_s^2\}$ from the results of one of his dynamo simulations. This work is partially supported by grant EAR-0309531 from the National Science Foundation.

REFERENCES

Acheson, D.J. & Hide, R., 1973. Hydromagnetics of rotating fluids, *Rep. Prog. Phys.,* **36,** 159–221.

Backus, G.E., 1983. Application of mantle filter theory to the magnetic jerk of 1969, *Geophys. J. R. astro. Soc,* **74,** 713–746.

Bloxham, J. & Gubbins, D., 1987. Morphology of the geomagnetic field and implications for the geodynamo, *Nature,* **325,** 509–511.

Bloxham, J. & Jackson, A., 1991. Fluid flow near the surface of Earths outer core, *Rev. Geophys.,* **29,** 97–120.

Bloxham, J. & Jackson, A., 1992. Time-dependent mapping of the magnetic field at the core-mantle boundary, *J. geophys. Res.,* **97,** 19 537–19 563.

Bloxham, J., Zatman, S. & Dumberry, M., 2002. The origin of geomagnetic jerks, *Nature,* **420,** 65–68.

Braginsky, S.I., 1970. Torsional magnetohydronamic vibrations in the Earth's core and variations in the length of day, *Geomag. Aeron., Engl. Transl.,* **10,** 1–8.

Braginsky, S.I., 1984. Short-period geomagnetic secular variation, *Geophys. Astrophys. Fluid Dyn.,* **30,** 1–78.

Buffett, B.A., 1996. A mechanism for decade fluctuations in the length of day, *Geophys. Res. Lett.,* **23,** 3803–3806.

Buffett, B.A., 1998. Free oscillations in the length of day: inferences on physical properties near the core-mantle boundary, in *The Core-Mantle Boundary Region,* Vol. 28, pp. 153–165, eds Gurnis, M., Wysession, M., Knittle, E., Buffet, B., AGU Geodynamics Monograph.

Buffett, B.A. & Mound, J.E., 2005. A Green's function for the excitation of torsional oscillations in the Earth's core, *J. geophys. Res.,* **110,** B08194, doi:10.1029/2004JB003495.

Buffett, B.A., Mathews, P.M. & Herring, T.A., 2002. Modeling of nutation and precession: effects of electromagnetic coupling, *J. geophys. Res.,* **107**(B4), 2070, doi:10.1029/2000JB000056.

Christensen, U.R., Olson, P. & Glatzmaier, G.A., 1998. A dynamo model interpretation of geomagnetic field structures, *Geophys. Res. Lett,* **25,** 1565–1568.

Courtillot, V., LeMouël, J.-L. & Ducruix, J., 1984. On Backus' mantle filter theory and the 1969 geomagnetic impulse, *Geophys. J. R. astr. Soc.,* **78,** 619–625.

Dumberry, M. & Bloxham, J., 2003. Torque balance, Taylor's constraint and torsional oscillations in a numerical model of the geodynamo, *Phys. Earth planet. Inter.,* **140,** 29–51.

Dumberry, M. & Mound, J.E., 2008. Constraints on core-mantle coupling from torsional oscillation normal modes, *J. geophys. Res.,* **113,** B03102, doi:10.1029/2007JB005135.

Gilbert, F. & Dziewonski, A.M., 1975. Application of normal mode theory to retrieval of structural parameters and source mechanisms from seismic spectra, *Philos. Trans. R. Soc. Lond. A,* **278,** 187–269.

Goldreich, P. & Keeley, D.A., 1997. Solar seismology. II. The stochastic excitation of the solar p-modes by turbulent convection, *Astrophys. J,* **212,** 243–251.

Gough, D.O. *et al.*, 1996. The seismic structure of the Sun, *Science,* **272,** 1296–1300.

Gross, R.S., 2001. A combined length-of-day time series spanning 1832–1997: LUNAR97, *Phys. Earth planet. Inter.,* **123,** 65–76.

Hills, R.G., 1979. Convection in the Earth mantle due to viscous shear at the core-mantle interface and due to large-scale buoyancy, *PhD thesis*, New Mexico State University, Las Cruces, New Mexico.

Hide, R., Boggs, D.H. & Dickey, J.O., 2000. Angular momentum fluctuations with the Earth's liquid core and torsional oscillations of the core-mantle system, *Geophys. J. Int.,* **143,** 777–786.

Holme, R., 1998. Electromagnetic core-mantle coupling II: probing deep mantle conductance, in *The Core-Mantle Boundary Region,*Vol. 28, pp. 139–151, eds Gurnis, M., Wysession, M., Knittle, E., Buffet, B., AGU Geodynamics Monograph.

Holme, R. & de Viron, O., 2005. Geomagnetic jerks and a high-resolution length-of-day profile for core studies, *Geophys. J. Int.,* **160,** 435–439.

Hulot, G., LeMouël, J.-L. & Wahr, J., 1992. Taking into account truncation problems and geomagnetic model accuracy in assessing computed flows at the core-mantle boundary, *Geophys. J. Int.,* **108,** 224–246.

Jackson, A., 1997. Time dependency of tangentially geostrophic core surface motion, *Phys. Earth planet. Inter.,* **103,** 293–311.

Jackson, A., 2003. Intense equatorial flux spots on the surface of the Earth's core, *Nature,* **424,** 760–763.

Jackson, A., Bloxham, J. & Gubbins, D., 1993. Time-dependent flow at the core surface and conservation of angular momentum in the coupled core-mantle system, in *Dynamics of Earth's Deep Interior,* **Vol. 72**, pp. 97–107, eds LeMouël, J.-L., Smylie, D.E., Herring, T.A., AGU Monograph.

Jackson, A., Jonkers, A.R.T. & Walker, M.R., 2000. Four centuries of geomagnetic secular variation from historical records, *Philos. Trans. R. Soc. Lond. A,* **358,** 957–990.

Jault, D., Gire, C. & LeMouël, J.-L., 1988. Westward drift, core motions and exchanges of angular momentum between the core and mantle, *Nature,* **333,** 353–356.

Jault, D., Hulot, G. & LeMouël, J.L., 1996. Mechanical core-mantle coupling and dynamo modelling, *Phys. Earth planet. Inter.,* **98,** 187–191.

LeMouël, J.L., 1984. Outer-core geostrophic flow and secular variation of Earth's geomagnetic field, *Nature,* **311,** 734–735.

Matsui, H. & Okuda, H., 2004. Development of a simulation code for MHD dynamo processes using the GeoFEM platform, *Int. J. Comp. Fluid Dyn.,* **18,** 323–332.

Maus, S. *et al.*, 2005. The tenth generation international geomagnetic reference field, *Geophys. J. Int.,* **161,** 561–565.

Mound, J.E. & Buffett, B.A., 2005. Mechanism of core-mantle angular momentum exchange and the observed spectral properties of torsional oscillations, *J. geophys. Res.,* **110,** B08103, doi:10.1029/2004JB003555.

Mound, J.E. & Buffett, B.A., 2006. Detection of a gravitational oscillation in length of day, *Earth planet. Sci. Lett.,* **243,** 383–389.

Pais, A. & Hulot, G., 2000. Length of day decade variations, torsional oscillation and inner-core super-rotation: evidence from recovered surface zonal flows, *Phys. Earth planet. Inter.,* **118,** 291–316.

Press, W.H., Teukolsky, S.A., Vetterling, W.T. & Flannery, B.P., 2007. *Numerical Recipes: The Art of Scientific Computing,* 3rd edn, Cambridge University Press, Cambridge, p. 1235.

Romanowicz, B., 2003. Global mantle tomography: Progress status in the past 10 years, *Ann Rev. Earth Planet. Sci.,* **31,** 303–328.

Roberts, P.H. & Scott, S., 1965. On the analysis of secular variation, 1, A hydromagnetic constraint: Theory, *J. Geomag. Geoelectr.,* **17,** 137–151.

Roberts, P.H., Yu, Z.J. & Russell, C.T., 2007. On the 60-year signal from the core, *Geophys. Astrophys. Fluid Dyn.,* **101,** 11–35.

Stephenson, F.R. & Morrison, L.V., 1995. Long-term fluctuations in the Earth's rotation - 700 BC to AD-1990, *Philos. Trans. R. Soc. Lond. A,* **351,** 165–202.

Vestine, E.H. & Kahle, A.B., 1968. The westward drift and geomagnetic secular change, *Geophys. J. R. astr. Soc.,* **15,** 29–37.

Voorhies, C.V., 1995. Time varying fluid flow at the top of Earth's core derived from Definitive Geomagnetic Reference Models, *J. geophys. Res.,* **100,** 10 029–10 039.

Wardinski, I., Holme, R., Asari, S. & Mandea, M., 2008. The 2003 geomagnetic jerk and its relation to the core surface flows, *Earth planet. Sci. Lett.,* **267,** 468–481.

Zatman, S. & Bloxham, J., 1997. Torsional oscillations and the magnetic field within the Earth's core, *Nature,* **388,** 760–763.

Zatman, S. & Bloxham, J., 1999. On the dynamical implications of models of B_s in the Earth's core, *Geophys. J. Int.,* **138,** 679–686.

APPENDIX A

The equation governing torsional oscillations describes an angular momentum balance for the fluid cylinders. It is customary to express the governing equation in terms of the Fourier transform of $u_{\rm f}(s,t)$, which we define by

$$\tilde{u}_{\rm f}(s,\omega) = \int_{-\infty}^{\infty} u_{\rm f}(s,t) {\rm e}^{{\rm i}\omega t}\, {\rm d}t. \tag{A1}$$

The governing equation becomes (Braginsky 1970)

$$\omega^2 m(s)\tilde{u}_{\rm f} + \frac{\partial}{\partial s}\left[\tau(s)\frac{\partial \tilde{u}_{\rm f}}{\partial s}\right] + {\rm i}\omega f(s) = 0, \tag{A2}$$

where the friction $f(s)$ depends on relative motion at the fluid–solid boundaries,

$$m(s) = 4\pi\rho s^3(z_{\rm f} - z_i) \tag{A3}$$

is the moment density of the cylinders, and

$$\tau(s) = 4\pi s^3(z_{\rm f} - z_i)\{B_s^2\}/\mu_0 \tag{A4}$$

is the magnetic tension due to the B_s component of the field. The brackets denote the average over the surface of cylinders and μ_0 is the permeability of free space. The half height of the cylinders, $z_{\rm f} - z_i$ is expressed in terms of the cylindrical radius by $z_{\rm f} = (r_{\rm f}^2 - s^2)^{1/2}$ and $z_i = (r_i^2 - s^2)^{1/2}$.

Additional equations are required to describe the angular velocity of the mantle $\tilde{u}_m$ and inner core $\tilde{u}_i$. The torques on the mantle and inner core include the friction at the fluid–solid boundaries and gravitational coupling between the inner core and mantle. Separate angular momentum equations for the mantle and inner core are given by

$$\omega^2 C_m \tilde{u}_m - \gamma(\omega)(\tilde{u}_m - \tilde{u}_i) - {\rm i}\omega \int_0^{r_{\rm f}} f_m(s)\, {\rm d}s = 0 \tag{A5}$$

$$\omega^2 C_i \tilde{u}_i + \gamma(\omega)(\tilde{u}_m - \tilde{u}_i) - {\rm i}\omega \int_0^{r_i} f_i(s)\, {\rm d}s = 0, \tag{A6}$$

where C_m and C_i are the moments of inertia of the mantle and inner core, respectively. The friction terms f_m and f_i are also specific to the mantle or inner-core boundaries.

Eqs (A2), (A5) and (A5) are discretized using a finite volume method. A brief outline of the approach is given in Buffett & Mound (2005). When the frequency dependence of the gravitational torque $\gamma(\omega)$ is approximated by (16), the discretized equations can be written in the form

$$(\omega^2 A_2 + \omega A_1 + A_0)\tilde{u} = 0, \tag{A7}$$

where $\tilde{u} = [\tilde{u}_{\rm f}(s_1), \tilde{u}_{\rm f}(s_2), \ldots, \tilde{u}_{\rm f}(s_n), \tilde{u}_m, \tilde{u}_i]$. The normal modes are defined by solving the eigenvalue problem in (A7) for ω_k and $\tilde{u}_k$. (Boundary conditions are built into the definition of the matrices A_0, A_1 and A_2.) The orthogonality condition for the normal modes can also be expressed in discrete form (Buffett & Mound 2005)

$$(\omega_k + \omega_j)\tilde{u}_j^T A_2 \tilde{u}_k + \tilde{u}_j^T A_1 \tilde{u}_k = \delta_{kj} \tag{A8}$$

which we use to normalize the modes.